Investigation of the secondary flow by convergent–divergent riblets in a supersonic turbulent boundary layer over a compression ramp

Tongbiao Guo, Jian Fang, Ji Zhang, and Xinliang Li

Published version information

Citation: T Guo et al. Investigation of the secondary flow by convergent–divergent riblets in a supersonic turbulent boundary layer over a compression ramp. Phys Fluids 34, no. 10 (2022): 106112

DOI: 10.1063/5.0123482

Physics of Fluids

Investigation of the secondary flow by convergent–divergent riblets in a supersonic turbulent boundary layer over a compression ramp

Cite as: Phys. Fluids **34**, 106112 (2022); https://doi.org/10.1063/5.0123482
Submitted: 30 August 2022 • Accepted: 29 September 2022 • Accepted Manuscript Online: 30 September 2022 • Published Online: 31 October 2022

Tongbiao Guo (郭同彪), Jian Fang (方剑), Ji Zhang (张吉), et al.

Physics of Fluids ARTICLE scitation.org/journal/phf

Investigation of the secondary flow by convergent–divergent riblets in a supersonic turbulent boundary layer over a compression ramp

Cite as: Phys. Fluids **34**, 106112 (2022); doi: 10.1063/5.0123482
Submitted: 30 August 2022 · Accepted: 29 September 2022 ·
Published Online: 31 October 2022

Tongbiao Guo (郭同彪),[1] Jian Fang (方剑),[2] Ji Zhang (张吉),[1,3] and Xinliang Li (李新亮)[1,3,a)]

AFFILIATIONS

[1]LHD, Institute of Mechanics, Chinese Academy of Sciences, Beijing 100190, China
[2]Scientific Computing Department, STFC Daresbury Laboratory, Warrington WA4 4AD, United Kingdom
[3]School of Engineering Science, University of Chinese Academy of Sciences, Beijing 100049, China

[a)]Author to whom correspondence should be addressed: lixl@imech.ac.cn

ABSTRACT

In this paper, the effect of the secondary flow induced by convergent–divergent riblets in supersonic turbulent boundary layers over a 24° compression ramp at Mach number 2.9 is studied via direct numerical simulation. Two riblet cases with the wavelength Λ being 1.1δ and 1.65δ (δ is the boundary layer thickness) are conducted to examine their impact on the secondary rolling motion, momentum transfer, turbulent fluctuations, flow separation, and unsteady shock motion. As the flow develops over the riblet section, both the size and intensity of the secondary rolling motion tend to increase. For the riblet case with $\Lambda/\delta = 1.1$, a single rolling mode is observed within a half wavelength, while a pair of co-rotating vortical structures is obtained for $\Lambda/\delta = 1.65$. Both rolling patterns lead to an apparent spanwise variation of the flow field. The results reveal that the secondary flow contributes to the increase of both the mean momentum flux and turbulent fluctuations. By using the spanwise averaging, the mean momentum flux contributed from the dispersive stress and compressible effect caused by the secondary flow is identified. Both components appear to enhance the near-wall momentum mixing, and a larger enhancement is observed for $\Lambda/\delta = 1.1$, where the intensity of the secondary flow is stronger. Compared to the baseline case, the area of the separation zone at $\Lambda/\delta = 1.1$ and $\Lambda/\delta = 1.65$ is decreased by 56% and 38%, respectively. For all the cases, the low-frequency motion near the foot of the shock is observed. In comparison, the frequency of the low-frequency motion for the riblet case is two times higher than that in the baseline case, owing to the reduction of the separation area and length.

I. INTRODUCTION

Shock wave/boundary layer interaction (SWBLI) occurs widely in high-speed internal and external flows of supersonic/hypersonic vehicles, such as the engine inlet, internal flow-path of scramjets, over-expanded nozzles, control surfaces, and so on. The resultant strong adverse pressure gradient can lead to flow separation, high wall heat flux, and strong pressure fluctuations, along with other complex physical phenomena.[1] It is, therefore, important to develop effective flow control methods to alleviate these detrimental effects.

The micro-ramp vortex generators (MVGs) have received great attention owing to their simplicity in implementation, strong robustness, and control effectiveness.[2] MVGs are capable of inducing large-scale streamwise vortices that increase the near-wall momentum by transporting the high-energy fluid in the outer part of the boundary layer to the near-wall region, enabling them to mitigate the flow separation caused by the shock-induced adverse pressure gradient. Nevertheless, with the increase of free-stream Mach number, the micro-vortex generators would be exposed to the high-speed outer flow, which brings a considerable amount of parasitic drag. Although a further decrease of the device height can hide MVGs in the low-speed inner flow and ease the increase of the parasitic drag, the controlling effect could be lost[2,3] with a height less than $0.1\delta_0$–$0.3\delta_0$ (δ_0 is the local boundary layer thickness). Rybalko *et al.*[3] reported that no control effect was obtained when the device height was decreased to $0.35\delta_0$ in the external compression low-boom inlets. As such, alternatives to conventional vortex generators, which are effective and simple to implement but only impose a negligible amount of parasitic drag, are highly desirable for high-speed applications.

Convergent–divergent (C–D) riblets are a new type of directional surface roughness patterns, which is inspired by the surface structures

of the sharks' skin[4] and the secondary flight feathers of birds.[5] For these surface patterns, sections of left-tilted and right-tilted riblets are arranged in an alternative manner in the spanwise direction, as seen in Fig. 1. In recent years, C–D riblets have received a large amount of research attention,[5–9] owing to their ability in performing the flow separation control[10–12] by producing large-scale streamwise vortices. The control mechanism of C–D riblets is similar to that of the MVGs, namely, enhancing the momentum transfer across the boundary layer by the large-scale secondary flow motion. In fact, C–D riblets could be regarded as a streamwise array of vortex generators with their height only a few percent of the local boundary layer thickness. It is the accumulative impact of these yawed riblets that produces the persistent streamwise vortical structures. Therefore, C–D riblets are expected to be an alternative device to the MVGs, with clear advantages in size and parasitic drag.

C–D riblets were first studied by Koeltzsch *et al.*[4] in a turbulent pipe flow. From their hot-wire measurements, they found that C–D riblets were capable of causing an apparent spanwise variation of the streamwise velocity and turbulent fluctuations in the circumferential direction. Later, Nugroho *et al.*[6] conducted an experimental study using hot-wire measurements in a turbulent boundary layer over C–D riblets, and they revealed a mean secondary rolling mode in the wall-normal-spanwise plane. Such a rolling mode is manifested by a downwelling that transports high-momentum fluid toward the wall and an upwelling that takes low-momentum fluid away from the wall. The presence of the rolling mode has also been observed in the stereoscopic particle image velocimetry experiments conducted by Kevin *et al.*[7] and Xu *et al.*[13] in turbulent boundary layer flows. Furthermore, Xu *et al.*[14] found that C–D riblets with a height of $2.4\%\delta_0$ brought a 50% increase in the turbulent shear stress and in the population of prograde/retrograde spanwise vortices over the converging region; in contrast, the impact of C–D riblets around the diverging region was weakened. Based on the flow database from Kevin *et al.*,[7] Bai *et al.*[15] reported that the large-scale secondary flow was associated with enhanced streamwise vortices and contributed to profound effects on the spatial correlations of velocity and the distributions of Reynolds stress. Guo *et al.*[9,16] carried out a parametric study of the effects of the riblet yaw angle and wavelength on the intensity of the secondary rolling mode in incompressible flow simulations. Their results indicated that the intensity of the secondary flow reached the peak when the yaw angle was around 45° and the wavelength was about one boundary layer thickness (or half channel height).[9,16]

Recently, Guo *et al.*[17] conducted a first direct numerical simulation (DNS) of a SWBLI to examine the impact of C–D riblets on the shock-induced flow separation. They found that with C–D riblets, the near-wall momentum around regions of down-welling was increased, and the separation area was significantly decreased. The opposite phenomenon occurs near regions of up-welling. They also pointed out that the Mach number around the region of up-welling was decreased, and the separation shock was also weaken,[18] which eased the enlargement of the separation area. In consequence, although the riblet height was only 3.3% of the boundary layer thickness, the area of the separation zone was reduced by 56%.

This paper is a follow-up research of our previous work[17] with an in-depth analysis of the evolution of the large-scale secondary flow induced by C–D riblets and its influence in a supersonic SWBLI. The key objectives are presented as follows.

(1) The streamwise evolution of the large-scale secondary flow is studied. To date, the existed study regarding C–D riblets is

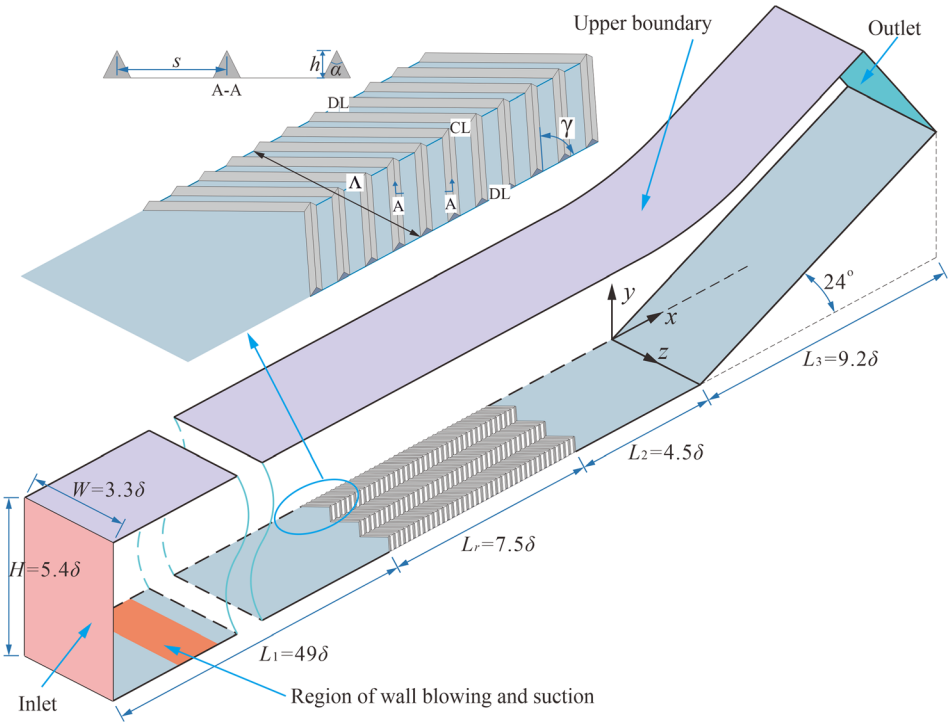

FIG. 1. Sketch of the computational domain with its local enlargement to illustrate the C–D riblets geometry parameters. Λ and γ are the riblet wavelength and yaw angle.

mainly focused on the flow characteristics in the wall-normal-spanwise plane, while the streamwise evolution of the large-scale streamwise vortices has been less reported. This is because, on the one hand, the experimental measurement is difficult to achieve the spatial development of the streamwise vortices. On the other hand, the existed numerical studies of turbulent flow over C–D riblets were mainly performed in channels,[9,19] in which the flow is homogeneous in the streamwise direction. Therefore, it is meaningful to explore how the large-scale rolling motion by C–D riblets is generated and developed.

(2) The momentum mixing that plays an important role in mitigating the flow separation is analyzed quantitatively. The intensity of the rolling motion by C–D riblets is much weaker than that by MVGs,[2] with the magnitude of the in-plane velocity lower than 3% of the free-stream velocity.[7,17] Thus, it is a valuable research to find out whether the weak rolling motion can enhance the momentum mixing. Based on double averaging operations (in time and space),[13,20] the contributions of turbulent fluctuations and the mean flux to the total momentum flux are obtained. Furthermore, the contributions of the dispersive stress and compression effect caused by the rolling motion to the mean momentum flux are achieved.

(3) The effect of the riblet's wavelength on the vortical structures is examined. C–D riblets have been reported to be able to induce two types of vortical structures within a half wavelength, i.e., a single streamwise rolling motion[7,13] and a pair of co-rotating vortical structures.[8,16] By conducting riblet cases with different riblet wavelength, the influence of the two kinds of vortical patterns on the momentum transfer and flow separation is examined.

(4) The effect of C–D riblets on the unsteady shock motion in the SWBLI system is analyzed. In our previous work,[17] the unsteady shock motion characteristics, such as the low-frequency motion of the shock, were not mentioned. This topic has attracted a large amount of research attention[21,22] and could be an interesting aspect to look into.

This paper is organized as follows. In Sec. II, the geometry of the C–D riblets is described in brief. Section III presents the results and discussions. Finally, conclusions are drawn in Sec. IV.

II. GEOMETRIC CONFIGURATION AND FLOW CONDITIONS

The present study is undertaken in a supersonic turbulent boundary layer with a 24° turning angle of the compression ramp at Mach number 2.9 via DNS. Figure 1 shows the geometric configuration of the computational domain. The streamwise, vertical, and spanwise directions are denoted by x, y, and z, respectively, and the corresponding velocity components are u, v, and w. δ is the boundary layer thickness at $x = -12\delta$ in the baseline case without C–D riblets and is used as the reference length. The enlarged drawing of C–D riblet parameters is shown in the top left part of Fig. 1. The acute angle that the micro-groove forms with the diverging line (DL) or converging line (CL) is called the yaw angle γ, and $\gamma = 45°$. The spanwise width of two adjacent DL or CL is the wavelength Λ. Riblets with trapezoidal cross-sections are used with the riblet height $h = \delta/30$ and riblet spacing $s = 4h$.

Three cases are simulated in this study, including one baseline case and two riblet cases with different sets of wavelength ($\Lambda = 1.1\delta$ and 1.65δ) to highlight the effect of Λ. The detailed descriptions of the numerical method and computational setup are given by Guo *et al.*[17]

In the following flow analysis, the Reynolds and density-weighted averaging operations are incorporated, which are, respectively, defined as $\bar{\phi} = (1/T)\int_T \phi dt$ and $\langle\phi\rangle = \overline{\rho\phi}/\bar{\rho}$ for a general variable ϕ. The fluctuations from the Reynolds and density-weighted averaging operations can be, therefore, expressed as $\phi' = \phi - \bar{\phi}$ and $\phi'' = \phi - \langle\phi\rangle$.

III. RESULTS AND DISCUSSION

In this section, the streamwise development of the secondary rolling motion induced by C–D riblets is first examined, followed by the analysis of the influence of the secondary flow on the mean flow field, momentum transfer, turbulent fluctuations, flow separation, and shock unsteadiness.

A. Spatial development of the secondary flow over riblets

The spatial development of the secondary flow in a turbulent boundary layer flow over C–D riblets with $\Lambda/\delta = 1.1$ is shown in Fig. 2 using the iso-surfaces of the mean-signed swirling strength $\Lambda_{ci} = -\lambda_{ci}\bar{\omega}_x/|\bar{\omega}_x|$. For the sake of brevity, results covering only one spanwise wavelength are presented. λ_{ci} is defined as the imaginary part of the complex–conjugate eigenvalue of the velocity gradient tensor,[23] and the mean streamwise vorticity ($\bar{\omega}_x = \frac{\partial\bar{w}}{\partial y} - \frac{\partial\bar{v}}{\partial z}$) is applied to denote the swirling direction. Here, $\Lambda_{ci} > 0$ and $\Lambda_{ci} < 0$ correspond to an anticlockwise and clockwise rotation, respectively. It can be seen from Fig. 2(a) that the secondary flow at the start of the riblet section appears mainly near the diverging/converging regions and the riblet grooves. As the secondary flow travels downstream, its size in the wall-normal direction tends to increase at a fast speed first and then it

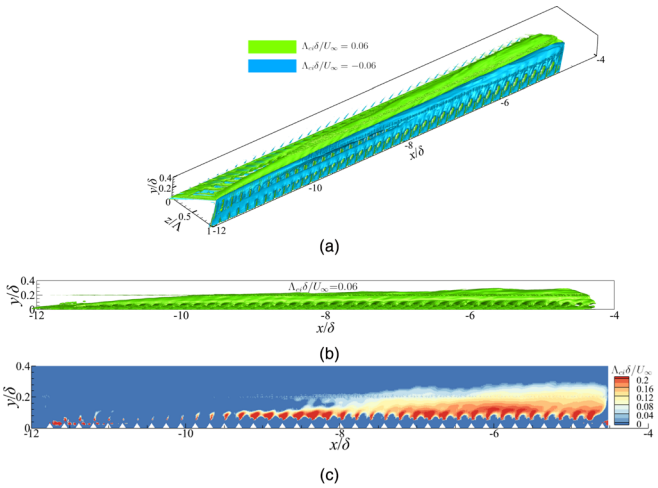

FIG. 2. Iso-surfaces of the time-averaged signed swirling strength with $\Lambda_{ci}\delta/U_\infty = 0.06$ and $\Lambda_{ci}\delta/U_\infty = -0.06$ along the streamwise direction in a turbulent boundary layer flow developing over C–D riblet section in the (a) 3D view and (b) side view, drawing the spatial development of swirling motion. (c) Contours of Λ_{ci} on the x–y plane at $z/\Lambda = 0.25$ (the mid-plane between the DL and CL). The results are for the riblet case with $\Lambda/\delta = 1.1$.

increases slowly [Figs. 2(a) and 2(b)]. It is noteworthy that the riblet geometry is symmetric with respect to the x–y plane over the DL or CL, and the resultant Λ_{ci} between two adjacent half wavelength regions has the same magnitude with opposite sign.

According to Fig. 2, one can see that both the size [Figs. 2(a) and 2(b)] and the intensity [Fig. 2(c)] of the vortical structures reveal riblet-scale fluctuations along the streamwise direction within one riblet spacing. In order to minimize the sensitivity of the result to the exact location of x and focus on the effect of the large-scale secondary flow, hereafter, streamwise averaging is performed over a streamwise length equivalent to one riblet spacing over the riblet section; for an arbitrary variable Θ, the streamwise averaging is expressed as follows:

$$\lfloor \Theta \rfloor_s(x,y,z) = \frac{1}{s/\sin(\gamma)} \int_{x-0.5s/\sin(\gamma)}^{x+0.5s/\sin(\gamma)} \Theta(x,y,z)dx, \tag{1}$$

where $s/\sin(\gamma)$ is the streamwise length of one riblet spacing, $\lfloor \cdot \rfloor_s$ denotes the streamwise averaging within one riblet spacing, and the symbol will be omitted in the following discussion for the sake of brevity.

To examine the vortical structures more closely, the contours of the mean-signed swirling strength in conjunction with in-plane velocity vectors on several cross-stream (y–z) planes are presented in Fig. 3. It is clear that the secondary rolling mode in Fig. 3 is owing to the inclined riblet grooves which induces the spanwise motion in the near-wall region from the DL to the CL. At all the y–z planes presented in Fig. 3, the strong intensity of Λ_{ci} is observed in the near-wall zone around the diverging region. This results from the strong downwash around the DL, which strikes the upstream facing side of the riblet valley and the fluid is defected upward and away from the DL. The phenomenon has also been observed in the incompressible flow via experiment[8] and numerical simulation.[16]

As the boundary layer develops over the ribbed surface in the streamwise direction, both the intensity of the swirling and the extent of the rolling motion tend to increase, and the large-scale rolling mode appears to dominate the vortical structures. Furthermore, as the flow moves downstream, the center of the circulating motion gradually moves away from the wall and toward the middle point between the converging and diverging lines. For example, at $x/\delta = -11.5$ [Fig. 3(a)], the rolling mode is confined near the ribbed wall within $y/\delta < 0.1$, and the center of the rolling mode lies at approximately $y/\delta = 0.04$. In contrast, at $x/\delta = -6$ [Fig. 3(d)], the rolling motion is extended to more than 40% of the boundary layer thickness, and a non-negligible intensity of the swirling is obtained up to $y/\delta = 0.3$.

Figure 4 presents contours of the time-averaged signed swirling strength and in-plane velocity vectors in the cross-stream plane at $x/\delta = -10$ and $x/\delta = -6$ for the riblet case with $\Lambda/\delta = 1.65$. In each cross-stream plane, there exists a pair of co-rotating vortical

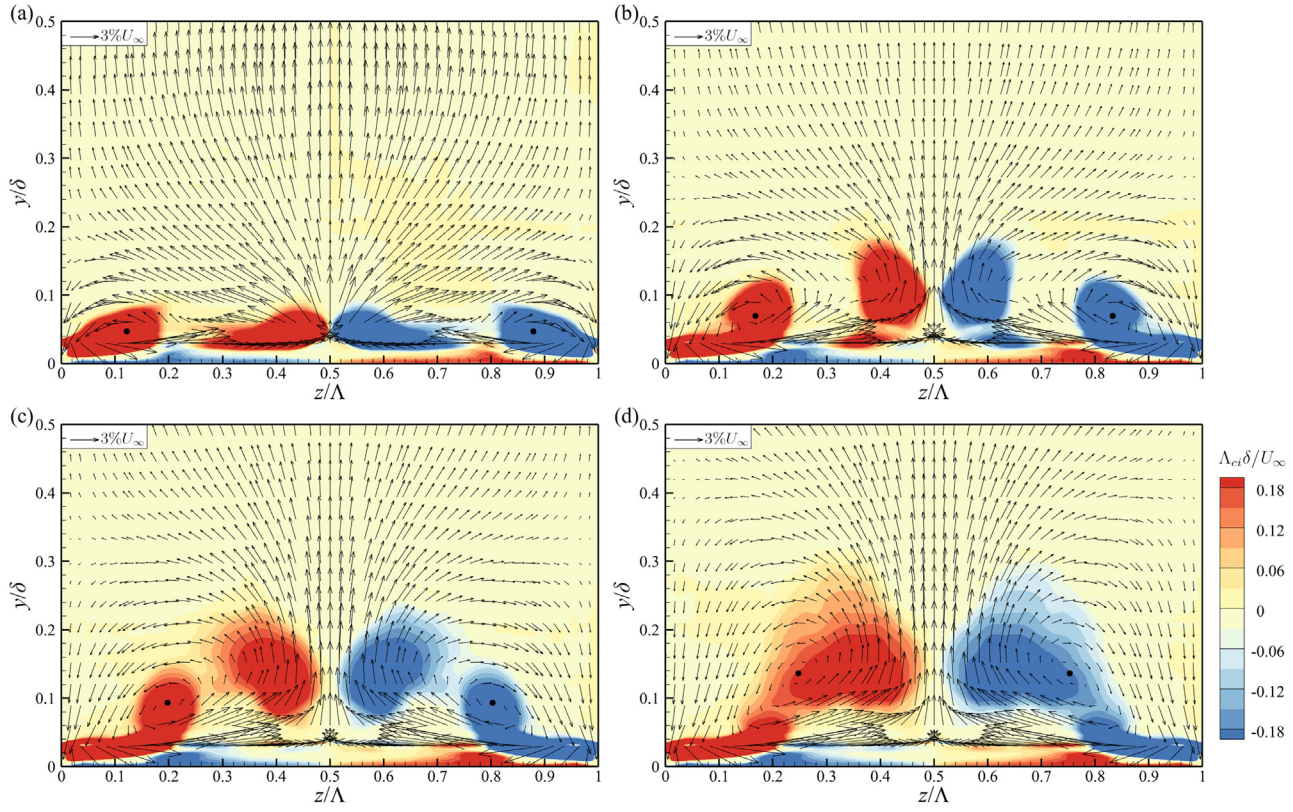

FIG. 3. Contours of the time-averaged signed swirling strength superimposed with the in-plane velocity vectors on the y–z planes at (a) $x/\delta = -11.5$, (b) $x/\delta = -10$, (c) $x/\delta = -8$, and (d) $x/\delta = -6$ for the riblet case with $\Lambda/\delta = 1.1$. The solid dot symbol indicates the center of the rolling motion. The streamwise averaging within one riblet spacing is performed using Eq. (1).

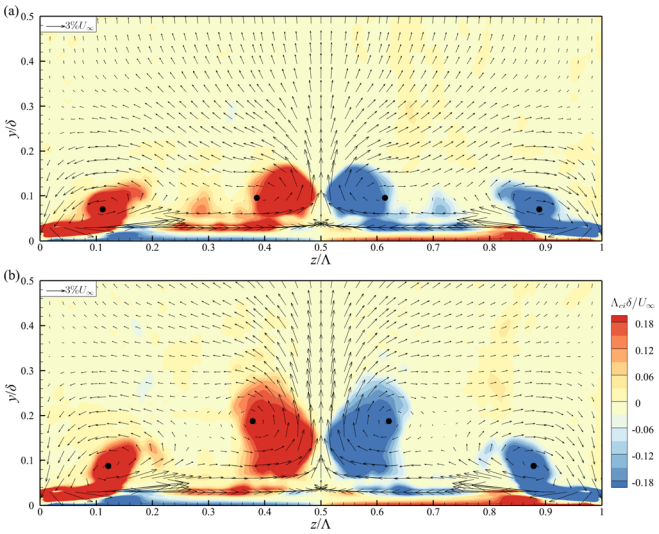

FIG. 4. Contours of the time-averaged signed swirling strength superimposed with the in-plane velocity vectors on the y–z planes at (a) $x/\delta = -10$ and (b) $x/\delta = -6$ for the riblet case with $\Lambda/\delta = 1.65$. The solid dot symbol indicates the center of the rolling motion.

structures over a half wavelength: one is located near the DL, and the other is closer to the CL. When the strong downwash strikes the riblet surface near the DL, the fluid is deflected upward and away from the DL, which is manifested by the inclined upward pointing in-plane velocity vectors near the DL over the riblet surface (Fig. 4). Under the combined influence of this local upward motion and the strong downwelling, a small local rolling mode is formed above the riblet grooves and very close to the DL. The other rolling mode on the right is caused by the global spanwise flow motion directing from the DL to the CL and the upwelling near the CL. Figure 5 shows the spatial development of the secondary flow for the riblet case with

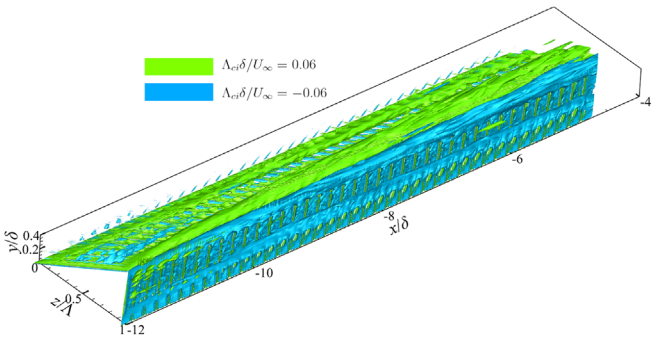

FIG. 5. Iso-surfaces of the time-averaged signed swirling strength with $\Lambda_{ci}\delta/U_\infty = 0.06$ and $\Lambda_{ci}\delta/U_\infty = -0.06$ along the streamwise direction in a boundary layer flow over C–D riblets in 3D view, drawing the spatial development of secondary flow for the riblet case with $\Lambda/\delta = 1.65$.

$\Lambda/\delta = 1.65$. Comparing Figs. 2(a) and 5, one can see that while for the riblet case with $\Lambda/\delta = 1.1$ the two separated regions with high swirling intensity tend to merge into one region as the flow travels downstream [Fig. 2(a)], they are not merged into one structure over the riblet section for $\Lambda/\delta = 1.65$ (Fig. 5), which is consistent with the observation of the swirling intensity in the y–z planes shown in Fig. 4.

To aid the quantitative comparison of the intensity of the secondary flow induced by C–D riblets, the spanwise-averaged intensity Γ_z and y–z plane-averaged value Γ_{yz} within the boundary layer are introduced as below:

$$\Gamma_z(x,y) = \frac{1}{0.5\Lambda}\int_{z=0}^{z=0.5\Lambda} \lfloor \Lambda_{ci} \rfloor_s \frac{\delta}{U_\infty} dz, \quad \Gamma_{yz}(x) = \frac{1}{\delta}\int_{y=0}^{y=\delta} \Gamma_z \, dy. \tag{2}$$

Figures 6(a) and 6(b) show the vertical distribution of Γ_z at a number of streamwise locations for the riblet cases. For the baseline case, Γ_z is zero and, hence, is not shown for brevity. One can see at

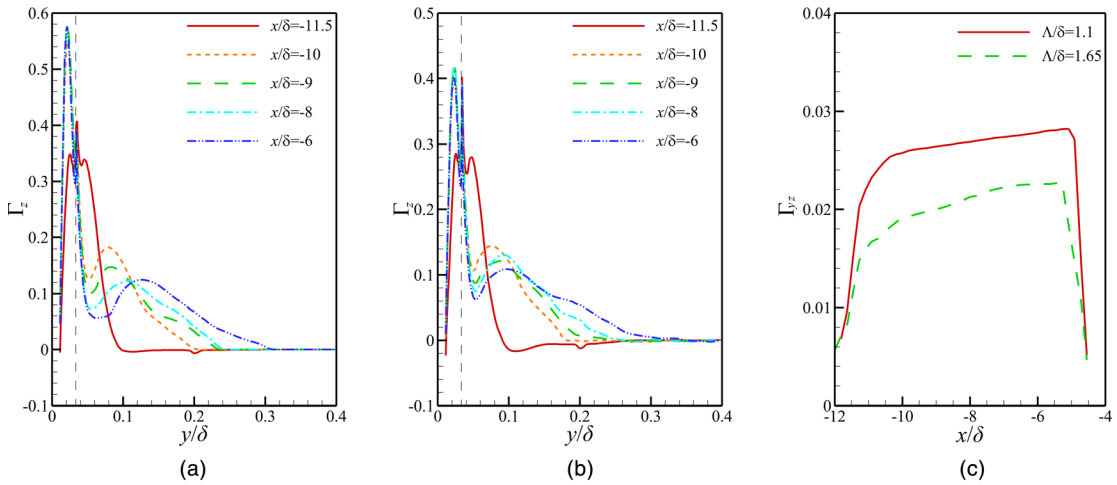

FIG. 6. Vertical distribution of Γ_z at a number of streamwise locations for the riblet cases with (a) $\Lambda/\delta = 1.1$ and (b) $\Lambda/\delta = 1.65$. (c) Streamwise distribution of Γ_{yz} for the two riblet cases.

$x/\delta = -11.5$, Γ_z is confined within $y/\delta < 0.1$, above which Γ_z is negligible. For other positions, there exists two apparent peaks of Γ_z: one is located inside riblet grooves, resulting from the strong downwelling and the resultant upwelling nearby; the other is located at the similar wall-normal position with the center of the rolling mode. As the flow develops over the ribbed surface in the streamwise direction, the latter peak of Γ_z appears to move away from the wall surface, and the edge of the rotational region moves from $y/\delta < 0.1$ at $x/\delta = -11.5$ to $y/\delta < 0.3$ at $x/\delta = -6$.

Figure 6(c) shows the streamwise distribution of Γ_{yz}. It can be seen that Γ_{yz} experiences a rapid increase at the beginning of the riblet section and then appears to increase at a relatively slower speed along the streamwise direction. Toward the end of the riblet section, the ability of C–D riblets in generating a spanwise flow directing from the DL to the CL is compromised due to the shortening of the grooves, leading to the decrease of Γ_{yz}. In comparison, the intensity of Γ_{yz} for the riblet case with $\Lambda/\delta = 1.1$ is larger than that with $\Lambda/\delta = 1.65$.

B. Impact of the secondary flow on the mean flow field

In Secs. III B-III F, the effect of the secondary flow induced by C–D riblets on the flow field is analyzed in detail. Hereafter, the physical parameters discussed are symmetric with respect to the x–y plane over the CL or DL. As such, results covering a half spanwise wavelength are presented for brevity.

Figure 7 presents contours of the mean fluid density on three y–z planes, i.e., $x/\delta = -10$, $x/\delta = -8$, and $x/\delta = -6$. The results of the baseline case are also provided for comparison. The upwelling around the CL takes the low-density fluid away from the wall, while the downward motion around the DL transports the high-density fluid toward the wall, leading to a spanwise variation of the density. From our previous study,[17] it was found that, in comparison with the baseline case, the streamwise velocity near the DL is increased and the opposite phenomenon occurs around the CL. In consequence, the near-wall fluid momentum near the DL/CL is increased/decreased, respectively. As the flow moves downstream over the riblet section, the secondary flow motion strengthens and begins to expand in the vertical direction, leading to stronger and larger spanwise variations of the fluid density and streamwise velocity.[17]

C. Momentum flux decomposition

Momentum transfer plays an important role in the ability of the flow in resisting adverse pressure gradient. In the compressible flow, the total momentum flux can be decomposed into contributions from the mean flow and turbulent fluctuations, i.e.,

$$-\overline{\rho u v} = -\bar{\rho}\langle u\rangle\langle v\rangle - \bar{\rho}\langle u''v''\rangle, \tag{3}$$

where the minus sign is added to ensure that the positive value denotes the enhancement of the near-wall momentum, and the following equation has been applied:

$$\overline{\langle u\rangle} = \langle u\rangle, \quad \overline{\rho u''} = \overline{\rho u} - \overline{\rho\langle u\rangle} = \overline{\rho u} - \overline{\rho(\overline{\rho u}/\overline{\rho})} = \overline{\rho u} - \overline{\rho u} = 0. \tag{4}$$

For an arbitrary variable Θ, the spanwise-averaged variables are denoted by the curly braces as

$$\begin{aligned} \Theta(x,y,z) &= \{\Theta\}_\Lambda(x,z) + \widehat{\Theta}(x,y,z), \\ \{\Theta\}_\Lambda(x,z) &= \frac{1}{\Lambda}\int_0^\Lambda \Theta(x,y,z)dy, \end{aligned} \tag{5}$$

where $\{\cdot\}_\Lambda$ represents the spanwise averaging within a spanwise wavelength; $\widehat{\cdot}$ denotes the dispersive component.[24,25]

The intensity of each term defined in Eq. (3) at $x/\delta = -6$ is presented in Fig. 8. In comparison to the baseline case, the total momentum flux for the C–D riblet cases is obviously larger in the near-wall region at $y/\delta < 0.4$. This helps increase the near-wall streamwise momentum, enabling it to mitigate the flow separation caused by the shock-induced adverse pressure gradient. In the region above about $y/\delta = 0.35$, the sign of the momentum flux $-\overline{\rho u v}$ changes from positive to negative, and the intensity for the riblet cases decreases at much faster speed than that of the baseline case, owing to the significantly increased vertical velocity caused by riblets.[17] It is worth emphasizing that in the region far away from the wall, the momentum flux is not as

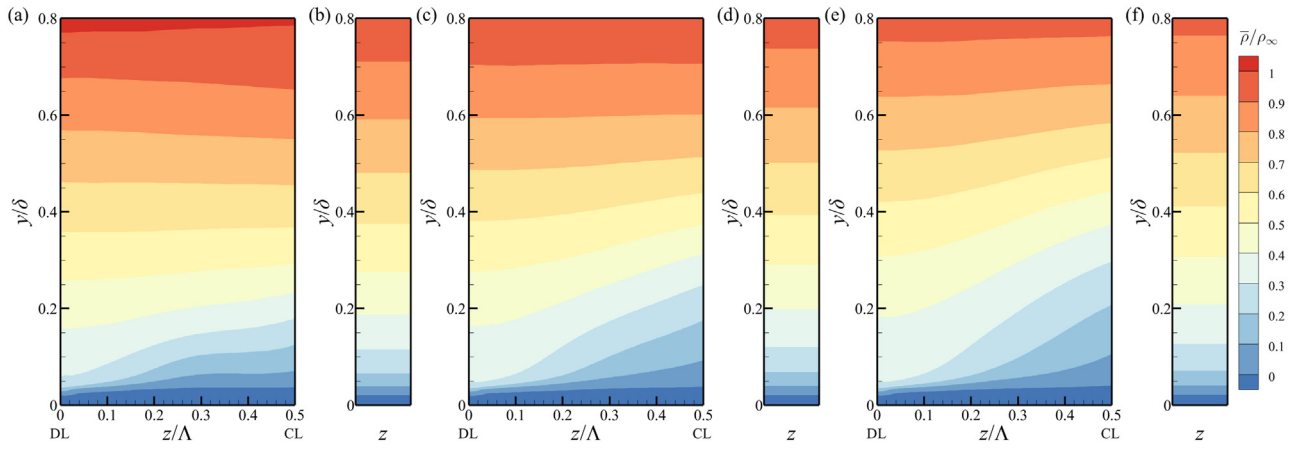

FIG. 7. Contours of the mean fluid density on the y–z planes at (a) and (b) $x/\delta = -10$; (c) and (d) $x/\delta = -8$; and (e) and (f) $x/\delta = -6$ for (a), (c), and (e) the riblet case with $\Lambda/\delta = 1.1$ and (b), (d), and (f) the baseline case.

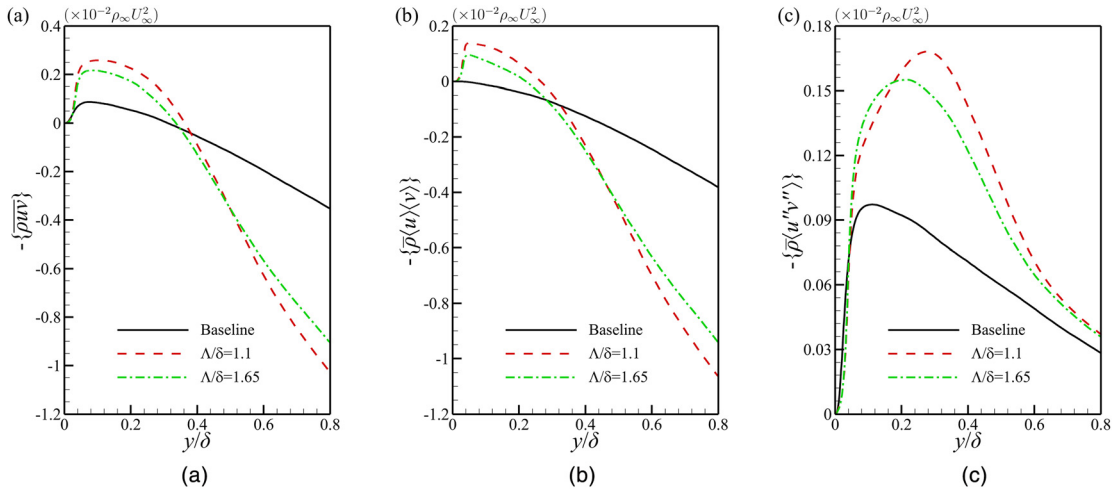

FIG. 8. Profiles of the spanwise-averaged (a) momentum flux and its components resulting from (b) the mean flow field and (c) turbulent fluctuations at $x/\delta = -6$, defined in Eq. (3).

important as that in the near-wall region since the corresponding streamwise momentum has been very high to avoid flow separation. From Fig. 8(b), one can see that $-\bar{\rho}\langle u\rangle\langle v\rangle$ for the baseline case is negative, indicating that the mean component weakens the ability in suppressing the flow separation. This is not surprising considering that the development of the flat plate boundary layer produces a positive vertical velocity. For the riblet cases, the induced secondary rolling mode contributes to a positive momentum flux at $y/\delta < 0.3$ with its intensity displaying the same trend as that of the secondary flow as Λ varies. Figure 8(c) compares the momentum flux arising from the turbulent fluctuations, and one can see that the riblet cases bring a much stronger $-\bar{\rho}\langle u''v''\rangle$ than that of the baseline case, and again, larger intensity of secondary rolling motion leads to stronger $-\bar{\rho}\langle u''v''\rangle$. This reason for the variation trend as Λ varies will be analyzed in detail below.

Comparing the variation trend of the swirling strength Γ_{yz} in Fig. 6(c) and the intensity of the mean momentum flux in Fig. 8(b) between the two riblet cases, the results imply a direct link between Γ_{yz} and $-\bar{\rho}\langle u\rangle\langle v\rangle$. To explore the physical mechanism for this consistent variation trend, the impact of the spanwise heterogeneity arising from the large-scale secondary flow on the mean momentum flux is analyzed here. Substituting Eq. (5) into Eq. (3) gives the expression for the mean momentum flux as

$$-\{\bar{\rho}\langle u\rangle\langle v\rangle\} = -\{\bar{\rho}\}\{\langle u\rangle\}\{\langle v\rangle\} - \{\bar{\rho}\}\{\widehat{\langle u\rangle\langle v\rangle}\} - \{\widehat{\bar{\rho}}\,\widehat{\langle u\rangle}\}\{\langle v\rangle\} - \{\widehat{\bar{\rho}}\,\widehat{\langle v\rangle}\}\{\langle u\rangle\} - \{\widehat{\bar{\rho}}\,\widehat{\langle u\rangle\langle v\rangle}\}, \quad (6)$$

where the first component on the right-hand side denotes the contribution from the spanwise-averaged flow field; the second term results from the disperse velocity;[24,25] the last three terms are relevant to the spanwise variation of the fluid density, resulting from the compressible effect with a non-zero $\widehat{\bar{\rho}}$ which is, hence, absent in the incompressible flow.[13,20]

The contributions of each component defined in Eq. (6) at $x/\delta = -6$ are presented in Fig. 9. It can be seen that the high intensity of the mean momentum flux at $y/\delta < 0.4$ results from the disperse velocity [Fig. 9(b)] and the compression effect with spanwise heterogeneous fluid density [Fig. 9(c)], which is a direct result of the downwelling/upwelling around the DL/CL caused by the secondary flow. In consequence, it is reasonable that Γ_{yz} and $-\bar{\rho}\langle u\rangle\langle v\rangle$ show the same variation trend as the wavelength varies. In comparison, the near-wall momentum flux is dominated by the $-\{\bar{\rho}\}\{\widehat{\langle u\rangle\langle v\rangle}\}$. This term refers to the dispersive stress and has been used to quantify the amount of the stress resulting from the spanwise heterogeneity of the velocity field in the incompressible flow.[24,25]

Figure 10 shows contours of the dispersive stress $-\{\bar{\rho}\}\widehat{\langle u\rangle\langle v\rangle}$ on four y–z planes for the riblet case with $\Lambda/\delta = 1.1$. The dispersive stress for the baseline case is zero and, hence, is not presented here. It can be clearly seen that as the flow develops over the riblet section, the intensity of $-\{\bar{\rho}\}\widehat{\langle u\rangle\langle v\rangle}$ appears to increase, and so does the area region with non-negligible dispersive stress. At $x/\delta = -11.5$, $-\{\bar{\rho}\}\widehat{\langle u\rangle\langle v\rangle}$ is only noticeable below $y/\delta = 0.12$, while the region with non-negligible $-\{\bar{\rho}\}\{\widehat{\langle u\rangle\langle v\rangle}\}$ extends to 45%δ at $x/\delta = -6$.

The contours of the dispersive stress $-\{\bar{\rho}\}\widehat{\langle u\rangle\langle v\rangle}$ on three y–z planes for the riblet case with $\Lambda/\delta = 1.65$ are presented in Fig. 11, to examine the influence of the riblet wavelength. One can see that as the wavelength increases to $\Lambda/\delta = 1.65$, the region with non-zero $-\{\bar{\rho}\}\{\widehat{\langle u\rangle\langle v\rangle}\}$ becomes more confined to the zone near the DL and CL, leaving a vast region across the mid-span with negligible $-\{\bar{\rho}\}\widehat{\langle u\rangle\langle v\rangle}$. This is because the flow across the mid-span is mainly parallel to the wall making little contribution to the momentum mixing, as seen in Fig. 4. As a result, the enhancement of momentum mixing resulting from the dispersive velocity for the riblet case at $\Lambda/\delta = 1.1$ is larger than that at $\Lambda/\delta = 1.65$.

D. Impact of the secondary flow on the turbulent fluctuations

Contours of the turbulence kinetic energy $\bar{\rho}\langle k\rangle$ and Reynolds shear stress $\bar{\rho}\langle -u''v''\rangle$ on three y–z planes, i.e., $x/\delta = -10$, $x/\delta = -8$,

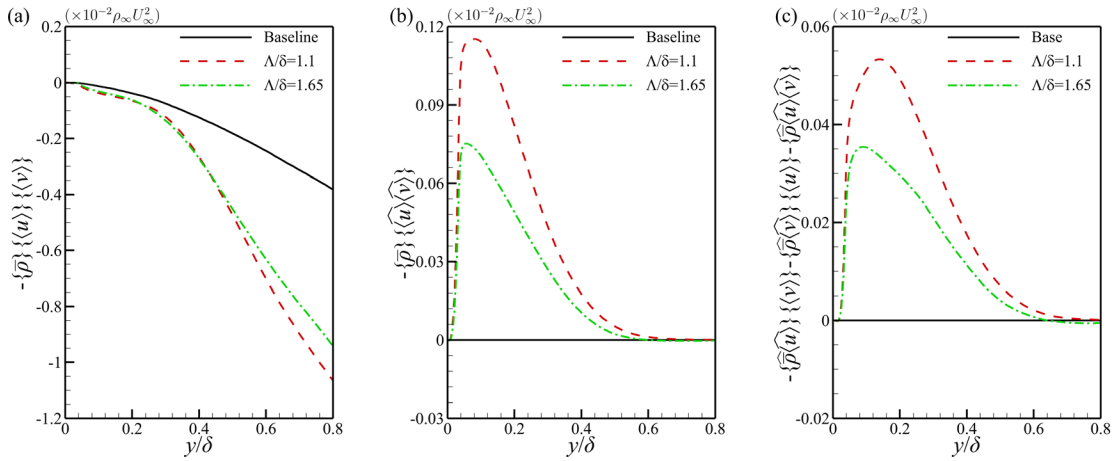

FIG. 9. Profiles of the spanwise-averaged mean momentum flux at $x/\delta = -6$ resulting from (a) spanwise-averaged flow field, (b) disperse velocity, and (c) compression effect with the spanwise heterogeneous fluid density, defined in Eq. (6).

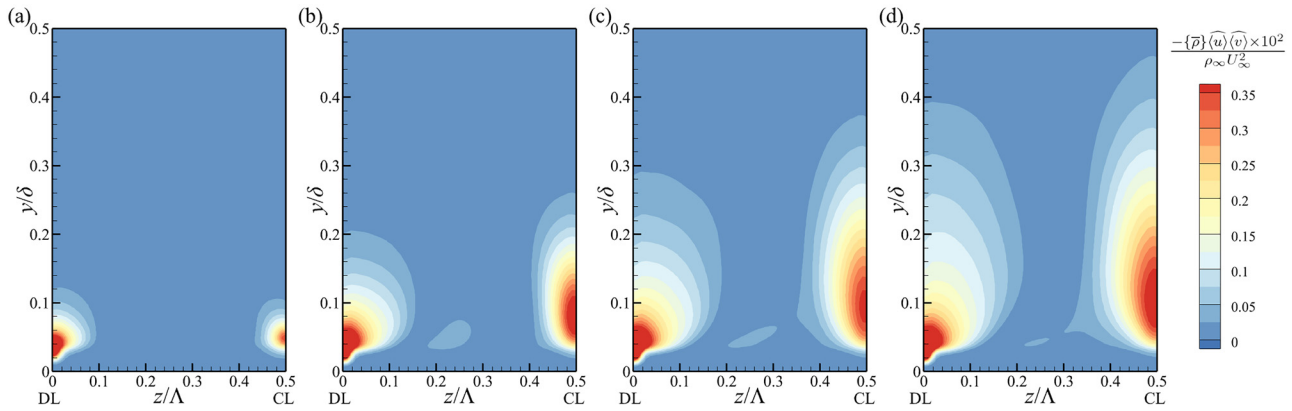

FIG. 10. Contours of the dispersive stress $-\{\bar{\rho}\}\widehat{\langle u\rangle}\widehat{\langle v\rangle}$ on y–z planes at (a) $x/\delta = -11.5$, (b) $x/\delta = -10$, (c) $x/\delta = -8$, and (d) $x/\delta = -6$ for the riblet case with $\Lambda/\delta = 1.1$.

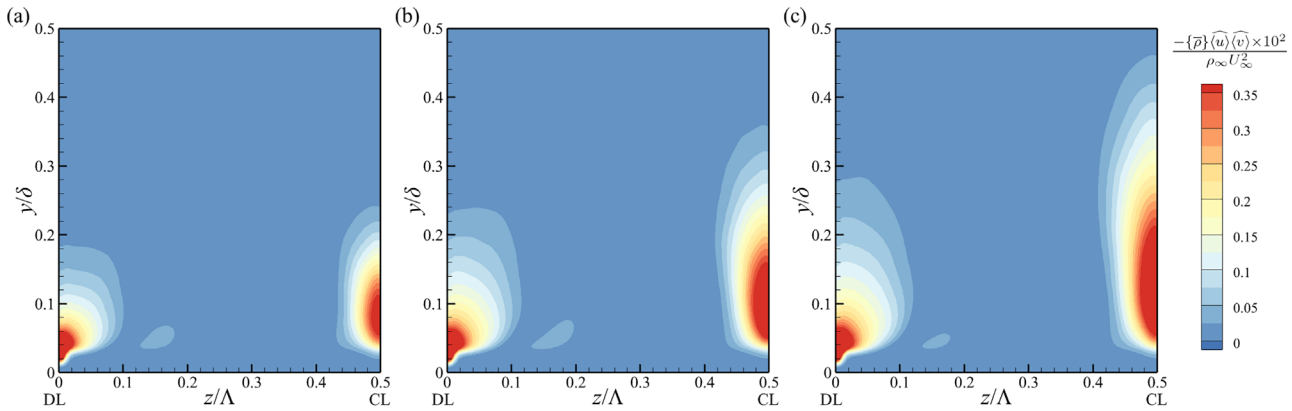

FIG. 11. Contours of the dispersive stress $-\{\bar{\rho}\}\widehat{\langle u\rangle}\widehat{\langle v\rangle}$ on y–z planes at (a) $x/\delta = -10$, (b) $x/\delta = -8$, and (c) $x/\delta = -6$ for the riblet case with $\Lambda/\delta = 1.65$.

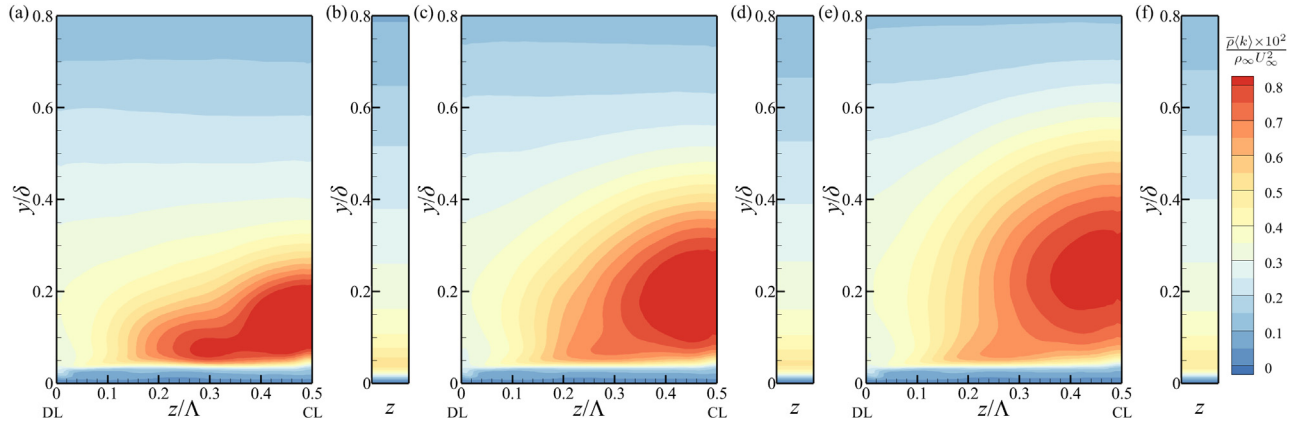

FIG. 12. Contours of the turbulence kinetic energy, $\bar{\rho}\langle k\rangle$, on the y–z planes at (a) and (b) $x/\delta = -10$; (c) and (d) $x/\delta = -8$; and (e) and (f) $x/\delta = -6$ for (a), (c), and (e) the riblet case with $\Lambda/\delta = 1.1$ and (b), (d), and (f) the baseline case.

and $x/\delta = -6$ are presented in Figs. 12 and 13 for the riblet case with $\Lambda/\delta = 1.1$. The results of the baseline case are also given for a reference. On the y–z plane, the area over the converging region has the highest intensity of $\bar{\rho}\langle k\rangle$ and $\bar{\rho}\langle -u''v''\rangle$, and such an area extends to a higher position as the flow moves downstream. This can be attributed to the increased upward motion of turbulence-rich fluid.[24]

To aid the quantitative comparison, Figs. 14(a) and 14(b) present profiles of the spanwise-averaged $\bar{\rho}\langle k\rangle$ and $\bar{\rho}\langle -u''v''\rangle$ at several streamwise positions for the riblet case with $\Lambda/\delta = 1.1$. In comparison with the baseline case, both $\bar{\rho}\langle k\rangle$ and $\bar{\rho}\langle -u''v''\rangle$ reveal an apparent increase at all the streamwise positions. As the flow moves downstream, the intensity of $\bar{\rho}\langle k\rangle$ and $\bar{\rho}\langle -u''v''\rangle$ for the baseline case shows little variation, and their intensity for the riblet case is significantly increased with their peak moving gradually away from the wall, resulting from the increased upwelling around the CL.

Figure 15 displays the contours of $\bar{\rho}\langle k\rangle$ and $\bar{\rho}\langle -u''v''\rangle$ on the y–z plane at $x/\delta = -6$ for the riblet case with $\Lambda/\delta = 1.65$. Compared to the results at $\Lambda/\delta = 1.1$, the impact of the upwelling on $\bar{\rho}\langle k\rangle$ and $\bar{\rho}\langle -u''v''\rangle$ becomes more confined to CL. In consequence, the spanwise-averaged intensity of $\bar{\rho}\langle k\rangle$ and $\bar{\rho}\langle -u''v''\rangle$ for the riblet case with $\Lambda/\delta = 1.1$ is larger than that at $\Lambda/\delta = 1.65$ [Figs. 14(c) and 8(c)]. In addition, there exists an additional local peak of both $\bar{\rho}\langle k\rangle$ and $\bar{\rho}\langle -u''v''\rangle$ for the riblet case with $\Lambda/\delta = 1.65$ near $z/\Lambda = 0.2$, which should be attributed to the local upwelling nearby (Fig. 4).

E. Impact of C–D riblets on the flow separation

Figure 16 shows contours of the separation height y_0, namely, the wall-normal distance between the iso-line with $\bar{u} = 0$ and the wall surface. The white lines represent the line with the mean skin friction coefficient $C_f = 0$, referring to the separation or reattachment lines. One can see that for all cases, the maximum y_0 occurs around the compression corner $x/\delta = 0$. In comparison with the baseline case, the separation height downstream of the DL for the riblet cases is significantly decreased, while y_0 downstream of the CL has an apparent increase, especially for the riblet case with $\Lambda/\delta = 1.65$. In consequence, the area of the spanwise-averaged separation zone for the riblet cases with $\Lambda/\delta = 1.1$ and $\Lambda/\delta = 1.65$ is decreased by 56% and 38%, respectively. The length of the separation zone can be quantified

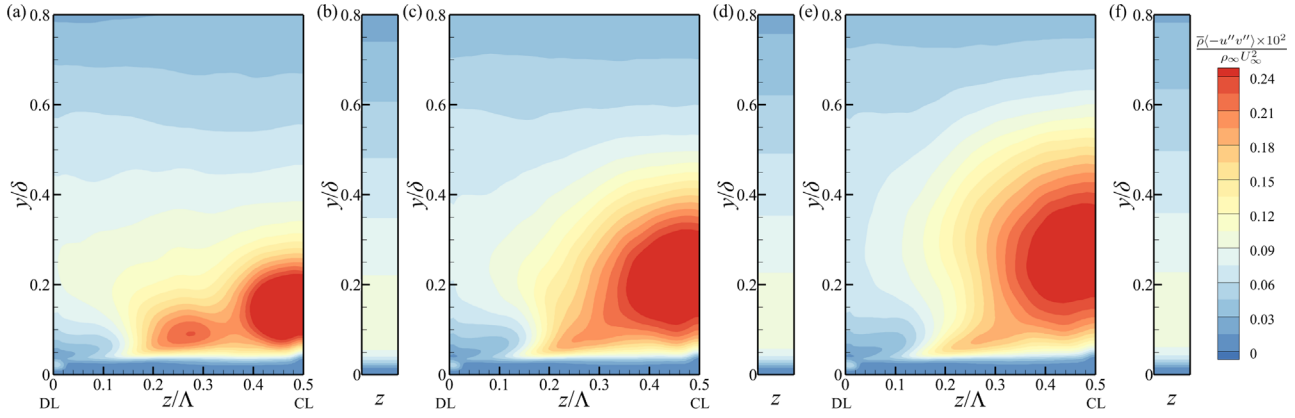

FIG. 13. Contours of the Reynolds shear stress, $\bar{\rho}\langle -u''v''\rangle$, on the y–z plane at (a) and (b) $x/\delta = -10$; (c) and (d) $x/\delta = -8$; and (e) and (f) $x/\delta = -6$ for (a), (c), and (e) the riblet case with $\Lambda/\delta = 1.1$ and (b), (d), and (f) the baseline case.

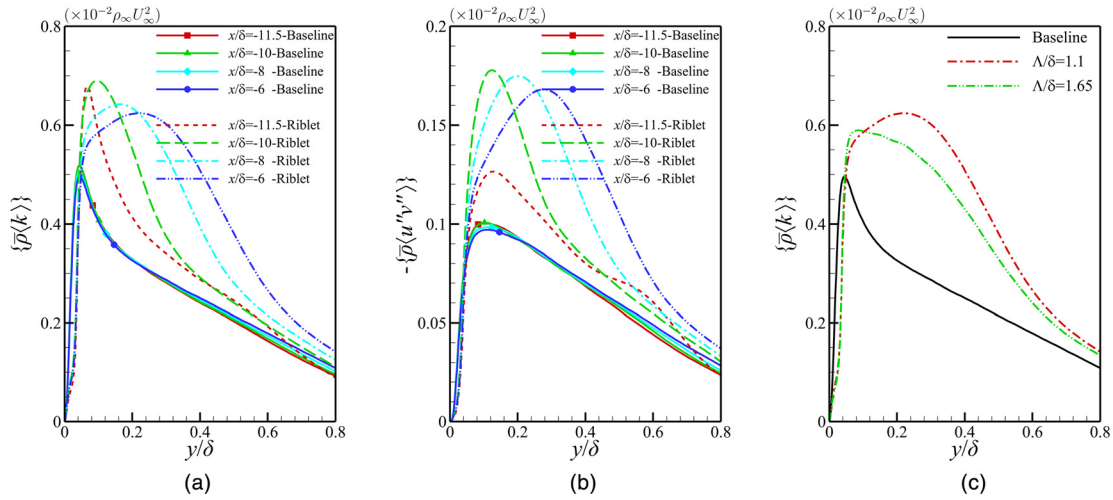

FIG. 14. Profile of the spanwise-averaged (a) and (c) $\bar{\rho}\langle k\rangle$ and (b) $\bar{\rho}\langle -u''v''\rangle$ (a) and (b) at several streamwise positions for the baseline and riblet case with $\Lambda/\delta = 1.1$; (c) for riblet cases with different wavelength at $x/\delta = -6$.

as the streamwise distance between the separation line and the reattachment line. From Fig. 16, one can see that, compared to the baseline case, the length of the separation zone downstream of the DL is shortened with an earlier reattachment, whereas the length downstream of the CL remains almost unchanged.

To illustrate the impact of C–D riblets on the flow separation quantitatively, the streamwise velocity profiles in the compression corner at different spanwise positions are presented in Fig. 17. For both riblet cases, there exists an apparent spanwise variation of $\bar{u}$ up to $y/\delta = 1.4$, especially for the riblet case with the larger wavelength. With a closer examination in the near wall region, $\bar{u}$ for the riblet cases is generally larger than that of the baseline case, especially at $y/\delta < 0.2$ where the reversed flow occurs.

Figure 18 reveals the main contributions of the momentum flux defined in Eqs. (3) and (6) at $x/\delta = -3.5$, the position slightly upstream of the separation line. As expected, the intensity of each component for the riblet case with $\Lambda/\delta = 1.1$ is higher, especially in the near-wall region. It has been reported that the net reduction of the separation area results from the large-scale rolling mode produced by C–D riblets that enhances the momentum mixing.[17] Consequently, it is reasonable that the riblet case with $\Lambda/\delta = 1.1$ performs better in suppressing the flow separation.

F. Impact of C–D riblets on the wall pressure in the interaction region

In this section, the impact of C–D riblets on unsteady characteristics of the wall pressure is examined, whereas only the baseline case and the riblet case with $\Lambda/\delta = 1.1$ are included since the flow characteristics between the two riblet cases are quite similar.

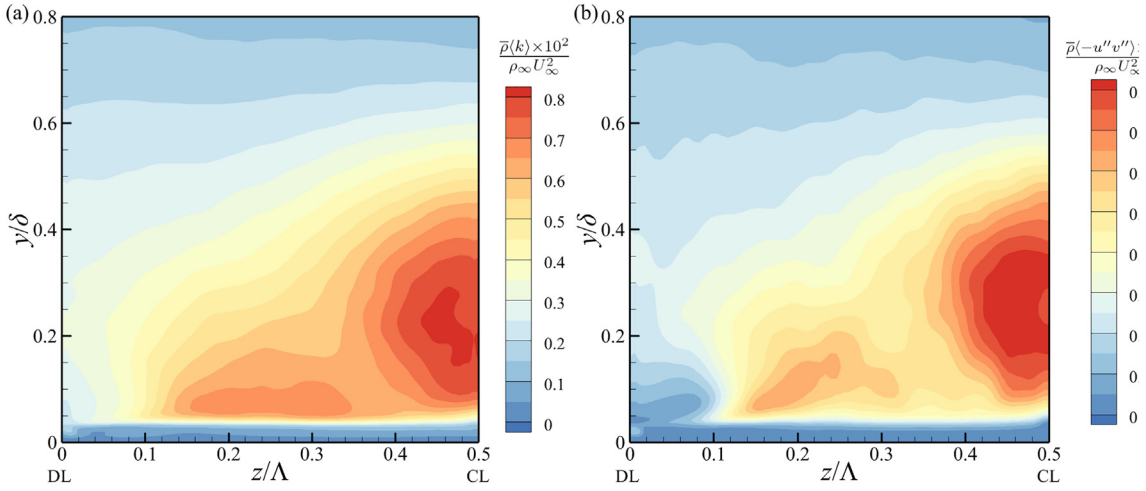

FIG. 15. Contours of (a) $\bar{\rho}\langle k\rangle$ and (b) $\bar{\rho}\langle -u''v''\rangle$ on the y–z plane at $x/\delta = -6$ for the riblet case with $\Lambda/\delta = 1.65$.

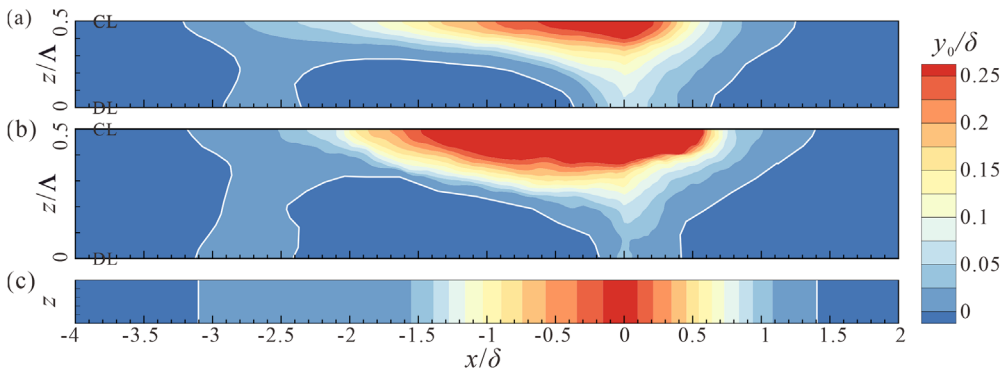

FIG. 16. Contours of the separation height y_0 for the riblet cases with (a) $\Lambda/\delta = 1.1$, (b) $\Lambda/\delta = 1.65$, and (c) the baseline case.

To study the unsteady motion of the shock wave, the intermittency factor, ζ, introduced by Dolling and Murphy[26] is used, which denotes the fraction time during which the wall pressure is above a threshold value, i.e.,

$$\zeta = \frac{\text{time}(p_w > (\bar{p}_{w,0} + 3\sigma(\bar{p}_{w,0})))}{\text{Total time}}, \tag{7}$$

where p_w represents the instantaneous wall pressure; $\bar{p}_{w,0}$ and $\sigma(\bar{p}_{w,0})$ represent the mean wall pressure and the corresponding standard deviation measured at the reference streamwise position $x/\delta = -12$ in the upstream undisturbed turbulent boundary layer. Figure 19 presents the streamwise distribution of ζ in the interaction zone for the riblet case over the DL/CL and that in the baseline case. The intermittency curves have the similar shape as those of Dolling and Murphy[26] and Tong *et al.*[27] In comparison with the baseline case, the profile shifts downstream toward the corner region for the riblet case. The variation trend is consistent with the finding reported by Tong *et al.*,[27] who found that the reduction of the separation area resulting from the decrease of the turning angle of the ramp contributes to the downstream movement of the intermittency curve. The streamwise length scale of the shock motion is calculated based on the streamwise length from $\zeta = 0.04$ to $\zeta = 0.99$. For the baseline case, the streamwise length is 0.98δ, while the corresponding values over the DL and CL are 0.87δ and 1.17δ, respectively.

The unsteady motion of the shock is characterized by a wide range of frequencies. To further illustrate the unsteadiness in the interaction region, contour of the weighted power spectral density ($WPSD = f * PSD(f)/\int PSD(f)df$, where PSD is the power spectral density of wall pressure) of the wall pressure is presented in Fig. 20, as a function of the dimensionless frequency $St_\delta = f\delta/U_\infty$ and the streamwise coordinate. For the baseline case, the most energetic frequency upstream of the interaction region is located around $St_\delta = 1.0$, which is a typical feature of the turbulent boundary layer.[21] As the flow approaches the beginning of the separation zone, the peak frequency shifts to lower frequencies associated with the shock motion, and then, it recovers back to $St_\delta = 0.5$ in the downstream flow.

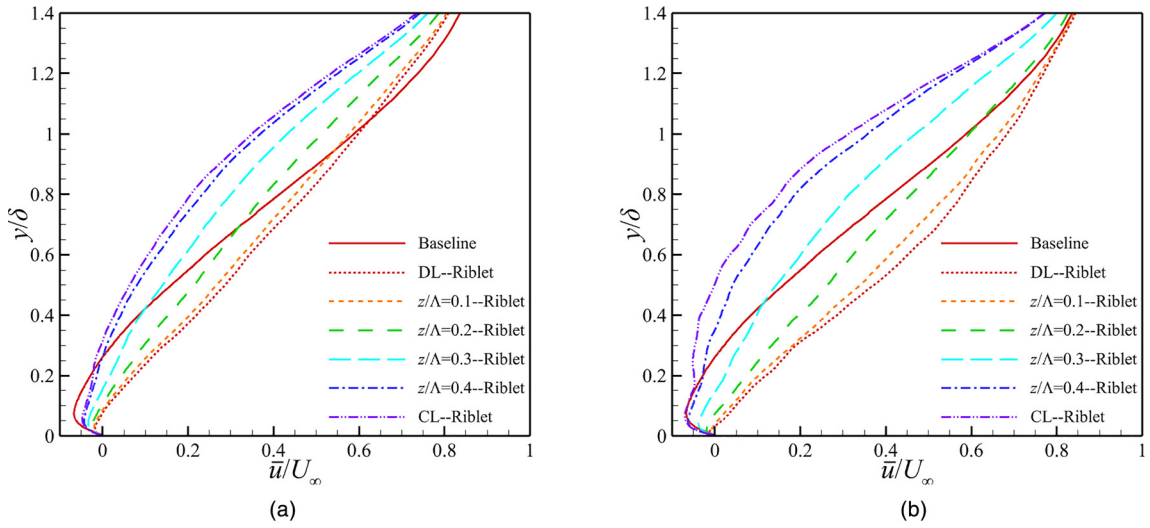

FIG. 17. Profiles of the streamwise velocity at $x/\delta = 0$ for the riblet cases with (a) $\Lambda/\delta = 1.1$ and (b) $\Lambda/\delta = 1.65$ at different spanwise positions. The result for the baseline case is also included for comparison.

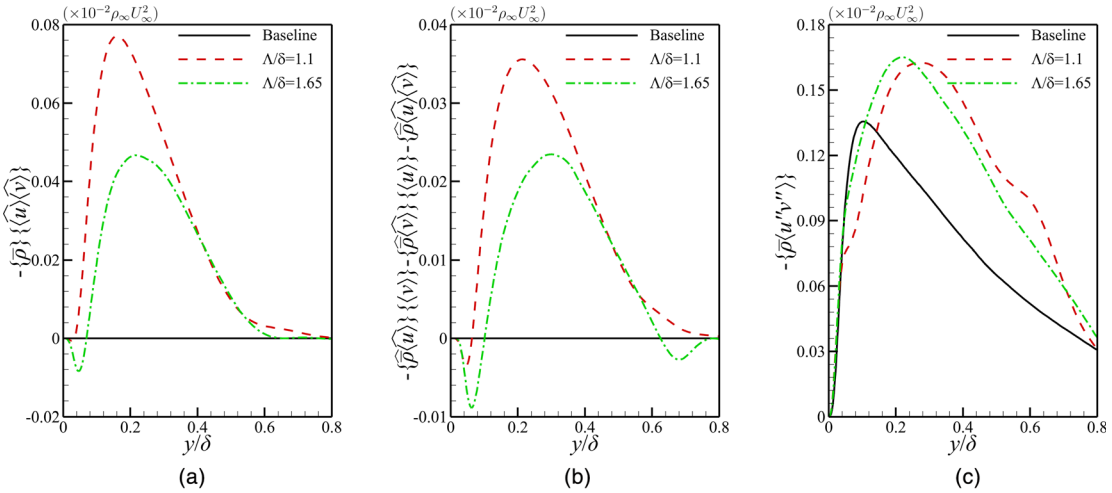

FIG. 18. Profiles of the spanwise-averaged mean momentum flux resulting from (a) the disperse velocity, (b) compressible effect with spanwise heterogeneous fluid density, and (c) Reynolds shear stress defined in Eqs. (3) and (6) at $x/\delta = -3.5$.

This behavior agrees well with the previous study by Priebe and Martín[21] and Grilli *et al.*[28] The phenomenon for the riblet case is quite similar except that there exist some streamwise variations scaled with the riblet's spacing upstream of the flow separation, resulting from the riblets. Near the separation point at $x/\delta = -3.0$, the energetic low-frequency for the baseline case is around $St_\delta = 0.004$, which is quite similar with the results by Grilli *et al.*[28] where $St_\delta = 0.0039$. In comparison, the energetic low-frequency for the riblet case is around $St_\delta = 0.008$. It has been reported that the energetic low-frequency scales with the separation length,[21] and the decrease of the separation length contributes to the increase of the low frequency f. In comparison with the baseline case, the flow separation length and area for the riblet case is significantly decreased (Fig. 16), and in consequence, St_δ corresponding to the energetic low-frequency is expected to increase. Comparing the low-frequency energy around $St_\delta = 0.008$ between the DL and CL, one can see that the value over the CL is much smaller,

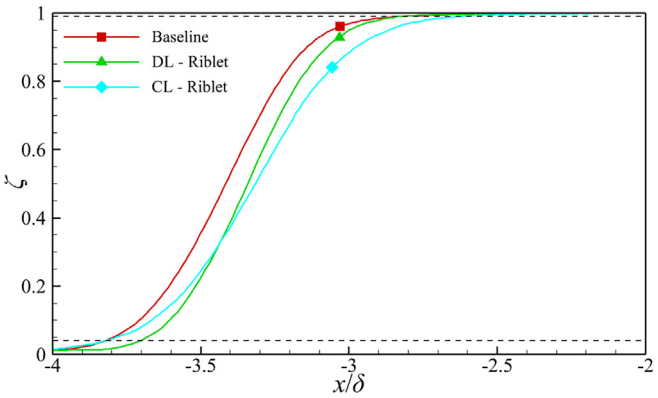

FIG. 19. Streamwise distribution of the intermittency factor ζ in the SWBLI region for the baseline case and the riblet case with $\Lambda/\delta = 1.1$ over the DL/CL. The dash line denotes the vertical position of $\zeta = 0.04$ and $\zeta = 0.99$.

resulting from the decreased local Mach number[17] that helps decrease the intensity of the local separation shock.[18]

IV. CONCLUSION

In this paper, the influence of the secondary rolling motion induced by C–D riblets in a supersonic turbulent boundary layer over a 24° compression ramp at Mach number 2.9 is studied via DNS. Two riblet cases with the wavelength Λ being 1.1δ and 1.65δ are conducted to examine the impact of the riblet wavelength. Since the secondary flows play a dominant role in the flow control, its spatial development in the supersonic turbulent boundary layer and its effect on the flow field momentum transfer, turbulent fluctuations, flow separation, and unsteady shock motion are analyzed in detail. Major findings are summarized as follows.

- As the boundary layer develops over the riblet section in the streamwise direction, the size and intensity of the secondary rolling motion increase at a fast speed first and then appear to increase slowly.
- For the riblet case with $\Lambda/\delta = 1.1$, a single rolling mode is observed within a half wavelength in the spanwise-wall-normal plane, while at $\Lambda/\delta = 1.65$, a pair of co-rotating vortical structures is obtained. In comparison, the intensity of the secondary flow for the riblet case with $\Lambda/\delta = 1.1$ is stronger.
- Both riblets cases contribute to a spanwise variation of the fluid density, turbulent fluctuations, and the momentum flux. Also, as the flow develops over the riblet section, the magnitude of the spanwise variation tends to increase.
- The total momentum flux is decomposed into contributions from the mean flux and turbulent fluctuations, both of which are increased by C–D riblets. Furthermore, the contribution of the mean momentum flux arising from the dispersive stress and compressible effect caused by C–D riblets increases the near-wall momentum mixing, and the increment is larger at $\Lambda/\delta = 1.1$ than that at $\Lambda/\delta = 1.65$.

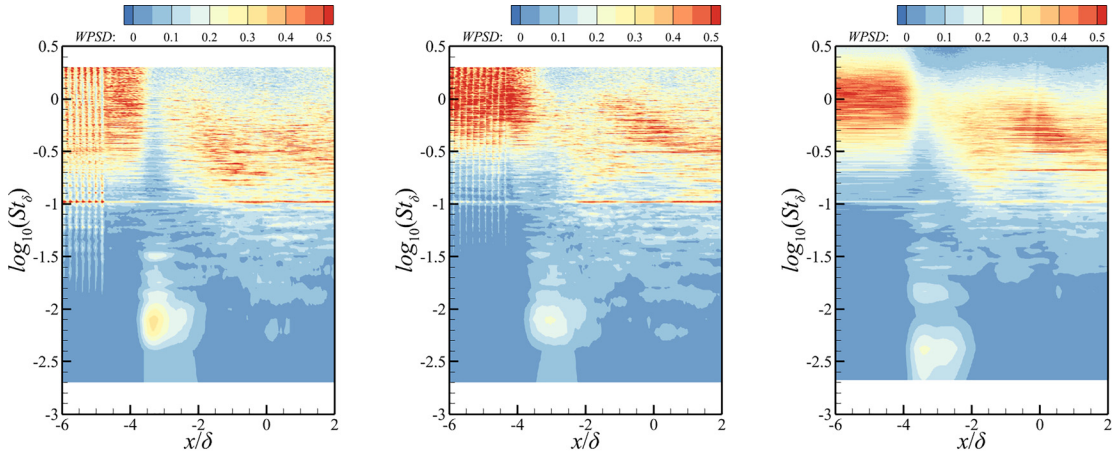

FIG. 20. Contours of the weighted power spectral density WPSD of the wall pressure in the interaction region for the riblet case over the (a) DL, (b) CL, and (c) the baseline case.

- The two riblet cases with different kinds of vortical structures are found to ease the flow separation. In comparison with the baseline case, the area of the separation zone for the riblet cases with $\Lambda/\delta = 1.1$ and $\Lambda/\delta = 1.65$ is decreased by 56% and 38%, respectively.
- For all cases, a low-frequency motion near the foot of the shock is observed, with a characteristic frequency that is three orders of magnitude lower than the typical frequency of the flat plat turbulent boundary layer. Compared to the baseline case, the frequency of the low-frequency motion for the riblet case with $\Lambda/\delta = 1.1$ is two times higher due to the reduction of the separation area and length.

ACKNOWLEDGMENTS

This work was supported by the National Key Research and Development Program of China (No. 2019YFA0405300); the National Natural Science Foundation of China (Nos. 12232018, 91852203, 12072349, and 12202457); and the GH fund A (No. 202202015832).

The authors thank the National Supercomputer Center in Tianjin (NSCC-TJ), and the National Supercomputer Center in GuangZhou (NSCC-GZ) for providing computer time.

Jian Fang acknowledges the UK Engineering and Physical Sciences Research Council (EPSRC) through the Computational Science Centre for Research Communities (CoSeC) and the UK Turbulence Consortium (No. EP/R029326/1).

AUTHOR DECLARATIONS

Conflict of Interest

The authors have no conflicts to disclose.

Author Contributions

Tongbiao Guo: Data curation (equal), Formal analysis (equal), Investigation (equal), Validation (equal), and Writing – original draft (equal). **Jian Fang:** Formal analysis (equal), Investigation (equal), Methodology (equal), and Validation (equal). **Ji Zhang:** Methodology (equal), Software (equal), and Validation (equal). **Xinliang Li:** Data curation (equal), Methodology (equal), Resources (equal), Software (equal), and Validation (equal).

DATA AVAILABILITY

The data that support the findings of this study are available from the corresponding author upon reasonable request.

REFERENCES

[1]D. S. Dolling, "Fifty years of shock-wave/boundary-layer interaction research: What next?," AIAA J. **39**, 1517–1531 (2001).
[2]A. G. Panaras and F. K. Lu, "Micro-vortex generators for shock wave/boundary layer interactions," Prog. Aerosp. Sci. **74**, 16–47 (2015).
[3]M. Rybalko, E. Loth, R. Chima, S. Hirt, and J. Debonis, "Micro-ramps for external compression low-boom inlets," AIAA Paper No. 2009-4206, 2009.
[4]K. Koeltzsch, A. Dinkelacker, and R. Grundmann, "Flow over convergent and divergent wall riblets," Exp. Fluids **33**, 346–350 (2002).
[5]H. Chen, F. Rao, X. Shang, D. Zhang, and I. Hagiwara, "Flow over bio-inspired 3D herringbone wall riblets," Exp. Fluids **55**, 1698 (2014).
[6]B. Nugroho, N. Hutchins, and J. Monty, "Large-scale spanwise periodicity in a turbulent boundary layer induced by highly ordered and directional surface roughness," Int. J. Heat Fluid Flow **41**, 90–102 (2013).
[7]K. Kevin, J. P. Monty, H. Bai, G. Pathikonda, B. Nugroho, J. M. Barros, K. T. Christensen, and N. Hutchins, "Cross-stream stereoscopic particle image velocimetry of a modified turbulent boundary layer over directional surface pattern," J. Fluid Mech. **813**, 412–435 (2017).
[8]F. Xu, S. Zhong, and S. Zhang, "Vortical structures and development of laminar flow over convergent-divergent riblets," Phys. Fluids **30**, 051901 (2018).
[9]T. Guo, J. Fang, S. Zhong, and C. Moulinec, "Energy-based drag decomposition analyses for a turbulent channel flow developing over convergent-divergent riblets," Phys. Fluids **34**, 025115 (2022).
[10]P. Quan, S. Zhong, Q. Liu, and L. Li, "Attenuation of flow separation using herringbone riblets at $M_\infty = 5$," AIAA J. **57**, 142–152 (2019).
[11]Q. Liu, S. Zhong, and L. Li, "Effects of bio-inspired micro-scale surface patterns on the profile losses in a linear cascade," J. Turbomach. **141**, 121006 (2019).

[12]T. Guo, S. Zhong, and T. Craft, "Control of laminar flow separation over a backward-facing rounded ramp with C-D riblets: The effects of riblet height, spacing and yaw angle," Int. J. Heat Fluid Flow **85**, 108629 (2020).
[13]F. Xu, S. Zhong, and S. Zhang, "Experimental study on secondary flow in turbulent boundary layer over spanwise heterogeneous microgrooves," Phys. Fluids **32**, 035109 (2020).
[14]F. Xu, S. Zhong, and S. Zhang, "Statistical analysis of vortical structures in turbulent boundary layer over directional grooved surface pattern with spanwise heterogeneity," Phys. Fluids **31**, 085110 (2019).
[15]H. Bai, J. Gong, and Z. Lu, "Energetic structures in the turbulent boundary layer over a spanwise-heterogeneous converging/diverging riblets wall," Phys. Fluids **33**, 075113 (2021).
[16]T. Guo, S. Zhong, and T. Craft, "Secondary flow in a laminar boundary layer developing over convergent-divergent riblets," Int. J. Heat Fluid Flow **84**, 108598 (2020).
[17]T. Guo, J. Fang, J. Zhang, and X. Li, "Direct numerical simulation of shock-wave/boundary layer interaction controlled with convergent-divergent riblets," Phys. Fluids **34**, 086101 (2022).
[18]M. Y. Ali, F. S. Alvi, R. Kumar, C. Manisankar, S. B. Verma, and L. Venkatakrishnan, "Studies on the influence of steady microactuators on shock-wave/boundary-layer interaction," AIAA J. **51**, 2753–2762 (2013).
[19]H. Benschop and W.-P. Breugem, "Drag reduction by herringbone riblet texture in direct numerical simulations of turbulent channel flow," J. Turbul. **18**, 717–759 (2017).
[20]V. Nikora, T. Stoesser, S. M. Cameron, M. Stewart, K. Papadopoulos, P. Ouro, R. McSherry, A. Zampiron, I. Marusic, and R. A. Falconer, "Friction factor decomposition for rough-wall flows: Theoretical background and application to open-channel flows," J. Fluid Mech. **872**, 626–664 (2019).
[21]S. Priebe and M. P. Martín, "Low-frequency unsteadiness in shock wave-turbulent boundary layer interaction," J. Fluid Mech. **699**, 1–49 (2012).
[22]K. M. Porter and J. Poggie, "Selective upstream influence on the unsteadiness of a separated turbulent compression ramp flow," Phys. Fluids **31**, 016104 (2019).
[23]J. Zhou, R. J. Adrian, S. Balachandar, and T. Kendall, "Mechanisms for generating coherent packets of hairpin vortices in channel flow," J. Fluid Mech. **387**, 353–396 (1999).
[24]C. Vanderwel, A. Stroh, J. Kriegseis, B. Frohnapfel, and B. Ganapathisubramani, "The instantaneous structure of secondary flows in turbulent boundary layers," J. Fluid Mech. **862**, 845–870 (2019).
[25]T. Medjnoun, C. Vanderwel, and B. Ganapathisubramani, "Effects of heterogeneous surface geometry on secondary flows in turbulent boundary layers," J. Fluid Mech. **886**, A31 (2020).
[26]D. S. Dolling and M. T. Murphy, "Unsteadiness of the separation shock wave structure in a supersonic compression ramp flowfield," AIAA J. **21**, 1628–1634 (1983).
[27]F. Tong, C. Yu, Z. Tang, and X. Li, "Numerical studies of shock wave interactions with a supersonic turbulent boundary layer in compression corner: Turning angle effects," Comput. Fluids **149**, 56–69 (2017).
[28]M. Grilli, P. J. Schmid, S. Hickel, and N. A. Adams, "Analysis of unsteady behaviour in shockwave turbulent boundary layer interaction," J. Fluid Mech. **700**, 16–28 (2012).